energy&fuels

Article

Cite This: Energy Fuels 2017, 31, 12288-12296

pubs.acs.org/EF

Mineral Particles in Sugar Cane Bagasse: Localization and Morphometry Using Microtomography Analysis

Daison Yancy-Caballero,[†,‡] Liu Y. Ling,[†] Nathaly L. Archilha,[§] João E. Ferreira,[‡] and Carlos Driemeier*[,†]

[†]Brazilian Bioethanol Science and Technology Laboratory (CTBE) and [§]Brazilian Synchrotron Light Laboratory (LNLS), Brazilian Center for Research in Energy and Materials (CNPEM), Campinas, São Paulo 13083-970, Brazil

[‡]Institute of Mathematics and Statistics (IME), University of São Paulo (USP), São Paulo, São Paulo 05508-090, Brazil

Supporting Information

ABSTRACT: Mineral particles are detrimental to lignocellulosic biomass utilization as fuel and feedstock of advanced biorefineries. Minerals may cause corrosion, sintering, and vitrification in boilers, gasifiers, and combustors as well as abrasion and erosion of mechanical equipment used in biomass processing. In this work, we employed synchrotron X-ray computed microtomography to analyze mineral particles in fibers of sugar cane bagasse, the vast lignocellulosic residue of the sugar cane industry. Hundreds of mineral particles with volumes from $\sim 10^2$ to 10^4 μm^3 were observed and analyzed. Mineral particles were found mostly in three regions of the biomass particles: (i) at external surfaces, (ii) at internal surfaces associated with tissue cracks, and (iii) inside parenchyma cells, which were ruptured for extraction of the sugar-rich juice. These results provide novel insights for the development of bagasse cleaning technologies aiming at improving feedstock quality for combustion and biorefining.

1. INTRODUCTION

The sugar cane industry has been a successful enterprise in several tropical and subtropical regions of the world. Despite technological and site-specific variables, the industry performs the following main operations.[1] Sugar cane stalks are harvested and transported to the mill. After biomass reception and some sort of cleaning, the stalks are shredded, aiming at opening the cells holding the sugar cane juice. This juice is extracted using either a diffuser or a series of roller mills. The sugar in the juice is then employed in the production of sugar and co-products, such as fuel ethanol. The fibrous residue left after crushing the stalks is the sugar cane bagasse.[2−4] Because bagasse is available in vast amounts at the processing site, bagasse is especially well-suited for energy purposes. Bagasse can be used as a solid fuel as well as a feedstock of advanced biorefineries producing cellulosic biofuels and co-products.[5−7]

Significant amounts of minerals are a well-known drawback for biomass usage as fuel. Minerals may cause severe problems of corrosion, sintering, and vitrification in boilers, gasifiers, and combustors.[8−11] The presence of inorganic constituents in combination with the elevated flue gas temperature leads to formation and volatilization of highly corrosive compounds that are deposited on reactor walls or heat exchanger surfaces in the form of a sticky layer. These compounds are produced mainly by the substantial amounts of alkali, potassium, sulfur, chlorine, and silica in the biomass. In addition, deposition of ash reduces the efficiency, performance, and utilization of equipment.

Besides lignocellulosic biomass usage directly as fuel, a range of new technologies is under development, from laboratory research to pioneer industrial facilities, aiming at converting the biomass into liquid biofuels and co-products.[5−7] The experience of the pioneer cellulosic ethanol facilities indicates that mineral impurities are also a major challenge for this industry beause minerals in biomass abrade and erode mechanical equipment, such as the screws feeding raw biomass into the pressurized zones of pretreatment reactors.[12]

Computed X-ray microtomography allows one to obtain three-dimensional (3D) images of solid specimens. Samples are illuminated by an X-ray beam, and the sample volume can be fully inspected non-invasively. Hence, the surface as well as the interior of the samples can be investigated without sectioning or any other complex sample preparation procedure. Microtomography can reach spatial resolution of ~ 1 μm or less. This scale is critical for analysis of plant biomass because cell wall thicknesses are at the micrometer scale. Therefore, X-ray microtomography has been employed in morphological studies of wood[13−15] as well as agricultural residues, such as sugar cane bagasse.[16]

In this work, we employ synchrotron X-ray microtomography to investigate mineral particles in sugar cane bagasse. Analysis of the 3D images reveals the sizes, shapes, and preferred location of mineral particles trapped in the bagasse structure. The results demonstrate that microtomography can provide analytical support for the development of novel biomass cleaning technologies. More specifically, the results of this pioneering study provide information for the development of new cleaning techniques for sugar cane bagasse used in energy and biorefining applications.

2. MATERIALS AND METHODS

2.1. Sampling of Bagasse Particles. The study was conducted with a bagasse sample collected from the bagasse conveyor belt of Usina da Pedra, Serrana, São Paulo, Brasil. Bagasse was air-dried and then stored in a sealed container. A total of 20 fibrous bagasse particles

Received: August 1, 2017
Revised: September 7, 2017
Published: October 27, 2017

DOI: 10.1021/acs.energyfuels.7b02247
Energy Fuels 2017, 31, 12288−12296

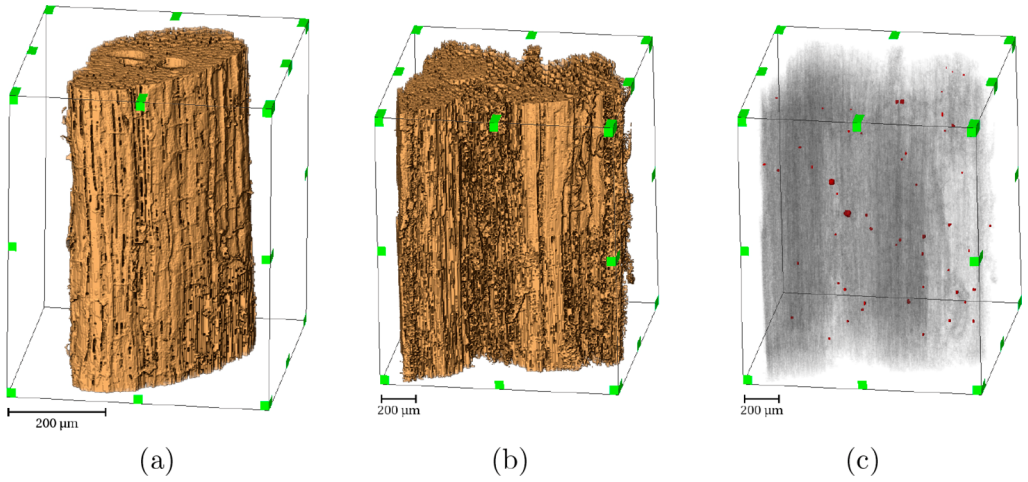

Figure 1. 3D visualizations of selected bagasse particles: (a) pith particle, (b) rind particle, and (c) segmented mineral particles in the rind particle.

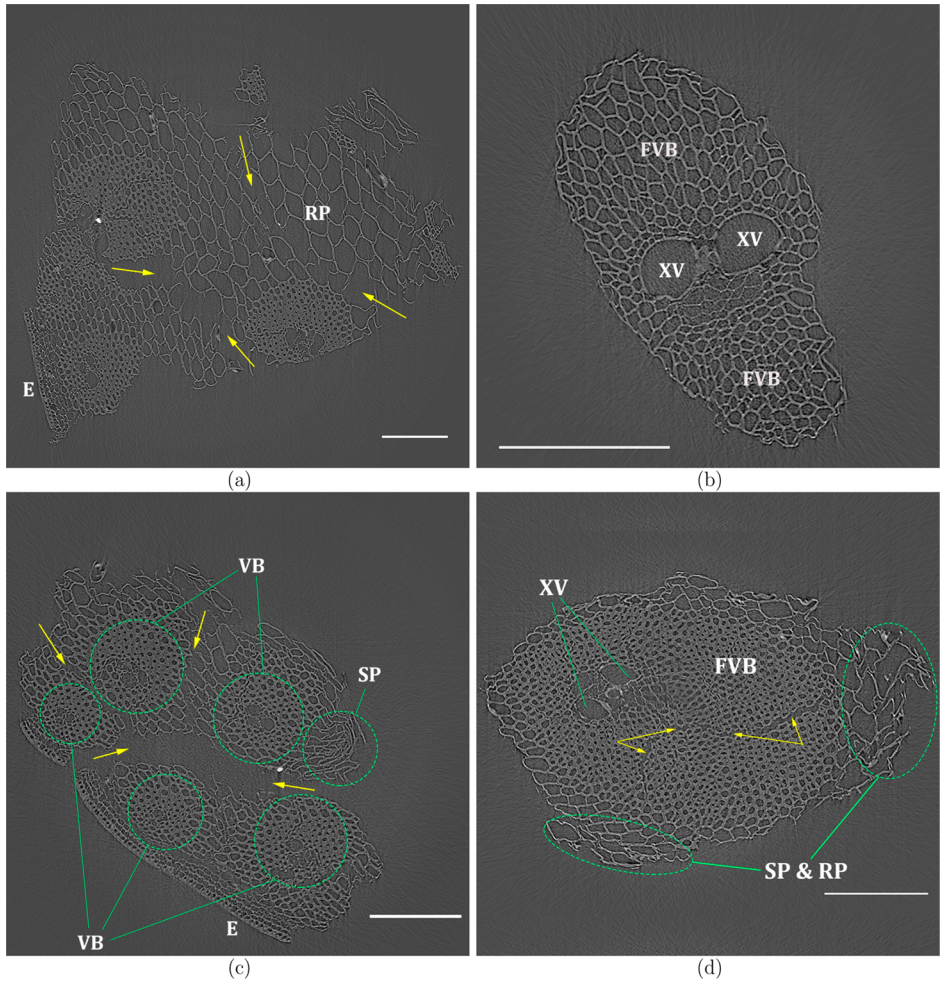

Figure 2. Selected 2D slices of 3D tomograms. The cross sections show (a) rind particle with four VBs, (b) pith particle with one VB, (c) rind particle with five VBs (circled with green), and (d) pith particle with one VB. Selected regions of round parenchyma (RP), smashed parenchyma (SP), fibers of vascular bundles (FVB), xylem vessel (XV), and epidermis (E) are indicated. Yellow arrows point to tissue cracks. Scale bars = 200 μm.

were selected for analysis. The particles must be mechanically self-sustained once attached to the base of the microtomography sample holder. Moreover, the particle lateral dimensions must fit into the microtomography field of view (1.68 mm × 1.68 mm). Because of these restrictions and bagasse heterogeneity,[2−4] particle selection was a biased process. We chose the analyzed particles to ensure that the most common bagasse particle types are represented, so that the microtomography analysis can produce valuable results and insights. Nevertheless, in quantitative terms, we cannot ensure that the images are statistically representative of the whole ensemble of bagasse particles.

DOI: 10.1021/acs.energyfuels.7b02247
Energy Fuels 2017, 31, 12288−12296

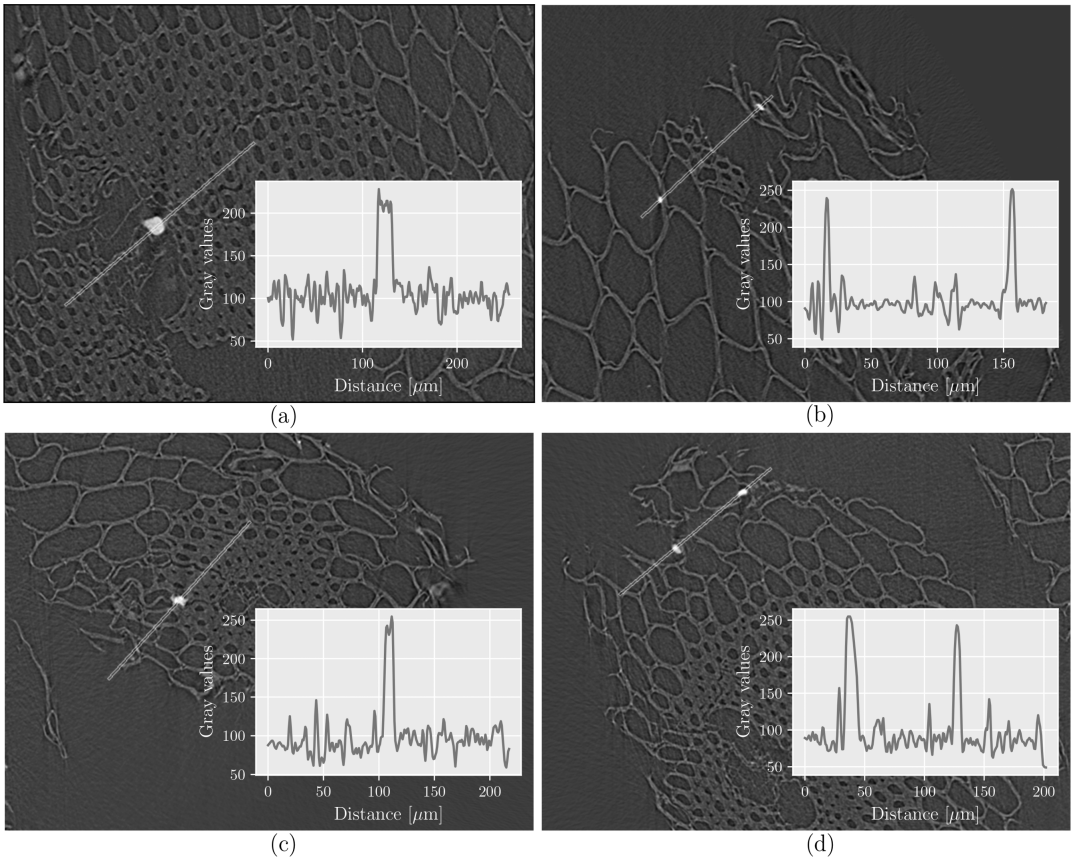

Figure 3. Examples of mineral particles in native grayscale images. The insets show grayscale profiles along the marked lines.

2.2. Image Acquisition and Reconstruction. X-ray microtomography images were acquired at the IMX beamline of the Brazilian Synchrotron Light Laboratory (LNLS).[17] The fibrous bagasse particles were fixed to the sample holder using modeling clay. The long axes of the fibrous particles were vertically aligned. Lateral dimensions of the bagasse particles were small enough to fit in the field of view of the detector, a PCO.2000 charge-coupled device (CCD) camera. On the other hand, the vertical dimensions exceeded the field of view in both directions; therefore, the analyzed volumes were away from the longitudinal extremes of the bagasse particles. For each 3D image, 1001 projection images were captured as the sample was rotated 180° around the vertical axis. Exposure times were varied (200−350 ms) to adjust to the decaying current of the synchrotron storage ring. A sample−detector distance of 269 mm and a 10× objective were employed. Phase contrast mode was used to enhance the material borders and ease the image segmentation. The full set of two-dimensional (2D) projections was mathematically converted into a 3D reconstruction using the PyHST software,[18,19] which employs filtered backprojection algorithms.[20,21] The reconstructed 3D images had a voxel size of 0.82 μm, with 2048 voxels (1.68 mm) in each one of the three spatial directions.

2.3. Classification of Bagasse Particles. Bagasse particles were classified in terms of the particle type and number of visible vascular bundles, which ranged from 1 to 5. Classification of bagasse particles was performed by visually inspecting each acquired 3D image. Three categories of particle type were considered: rind, pith, and undetermined. If the observed vascular bundles and parenchyma cells were associated in the way characteristic of sugar cane stalk internode, the particle was classified as either rind (with a visible epidermis) or pith (without a visible epidermis). A few particles showed very different morphology, likely originating from sugar cane tops, leaves, or any other vegetal impurities; their category of particle type was undetermined.

2.4. Mineral Particle Segmentation. Image processing was carried out with the Fiji[22] distribution of ImageJ.[23] In particular, mineral particle segmentation was performed using Python scripts that call functions of the Morphological Segmentation plugin from the MorphoLibJ library.[24] Images were preprocessed with a 3D Gaussian filter with σ = 2.0 in each spatial direction. Segmentation was performed with the plugin options for object image, using a morphological gradient with a radius of 1 and connectivity of 6. The dynamic value (tolerance) was varied between 15 and 25, and the optimal value of 21 was obtained, as detailed later in the paper. Details about the implementation of the Morphological Segmentation in Python scripts are given in the Supporting Information.

2.5. Mineral Particle Morphometry. Morphometry of the segmented mineral particles was performed with the MorphoLibJ[24] library. For specific verifications, the 3D ImageJ Suite library[25] was also employed (see the Supporting Information). Mineral particle morphometry considered only those particles completely inside the image volume; i.e., particles touching the image boundary were neglected. The following particle size metrics were calculated: volume, surface area, and semi-axis lengths (R_1, R_2, and R_3) of the greatest ellipsoid that fits inside the mineral particle.

In addition, the following shape metrics were calculated: sphericity (or compactness = sphericity^3), elongation, flatness, and ellipsoid factor (EF). Sphericity is defined as the ratio between the surface area of a sphere with the same volume of the particle and the surface area of the particle itself. The elongation index is the ratio between the major (R_1) and intermediate (R_2) axis lengths, while the flatness index is the ratio between the intermediate (R_2) and minor (R_3) axis lengths.[26] The EF is given by EF = $R_3/R_2 - R_2/R_1$, ranging from −1 for strongly oblate (disk-shaped) ellipsoids to +1 for strongly prolate (rod-shaped) ellipsoids.[27,28]

2.6. Localization of Mineral Particles. Mineral particle localization was conducted by highlighting the segmented mineral particles and then visually inspecting the 2D sections close to the centroid of

DOI: 10.1021/acs.energyfuels.7b02247
Energy Fuels 2017, 31, 12288−12296

each mineral particle. Localization was classified in terms of macrolocalization and cell type. Three categories of macrolocalization were considered: external biomass surface, internal surface associated with cracks in the biomass particle, and tissue interior. As per cell type, the following categories were considered: parenchyma cells with a round shape, parenchyma cells with a collapsed (smashed) shape, fibers in vascular bundles, xylem vessels, epidermis region, and undetermined.

3. RESULTS AND DISCUSSION

3.1. Overview of Bagasse Particles. Exemplary 3D visualizations of bagasse particles (panels a and b of Figure 1 and videos in the Supporting Information) show some surface irregularities as well as surface flakes and burrs, which are cell wall fragments still attached to the particle main body. However, the bagasse particles are relatively homogeneous along the fiber axis. Most of the variability is observed in the particle cross sections (Figure 2), which typically show vascular bundles (VBs) associated with parenchyma cells. In the rind particles, the epidermis can be noted (panels a and c of Figure 2). Moreover, cracks in tissues are also commonly observed (panels a, c, and d of Figure 2).

Table 1. Matrix of Bagasse Particle Types[a]

	number of VBs in the bagasse particle					
type of bagasse particle	1	2	3	4	5	total
rind	0	2	1	1	2	6
pith	8	2	1	0	0	11
undetermined	1	2	0	0	0	3
total	9	6	2	1	2	20

[a]Each one of the 20 bagasse particles was classified in terms of the type of bagasse particle and the number of VBs visualized in the particle cross section.

Classification of the analyzed bagasse particles resulted in 6 rind, 11 pith, and 3 particles of undetermined type (Table 1). The number of VBs in each pith particle ranges from 1 to 3, with 8 of the 11 pith particles showing a single VB. Rind particles are known to be larger and mechanically more robust, with a tighter association of VB, parenchyma, and epidermis regions. Indeed, the classification of Table 1 shows that the number of VBs is higher in the rind particles, ranging from 2 to 5 VBs per particle. As mentioned, the analyzed particles cannot be considered statistically representative of the whole bagasse. Nevertheless, the main types of fibrous particles and their typical features are represented in Table 1 and Figure 2. Only parenchyma disassociated from vascular bundles is absent from our microtomography analysis. Disassociated parenchyma makes a large fraction of the bagasse fines, but such a fraction does not stay self-sustained for the image acquisition.

3.2. Mineral Particle Segmentation. Before discussing the image analysis of mineral particles, let us briefly make some considerations about minerals in biomass. Minerals can be distributed throughout the cell walls as well as localized in mineral particles. For example, in an analysis of maize biomass

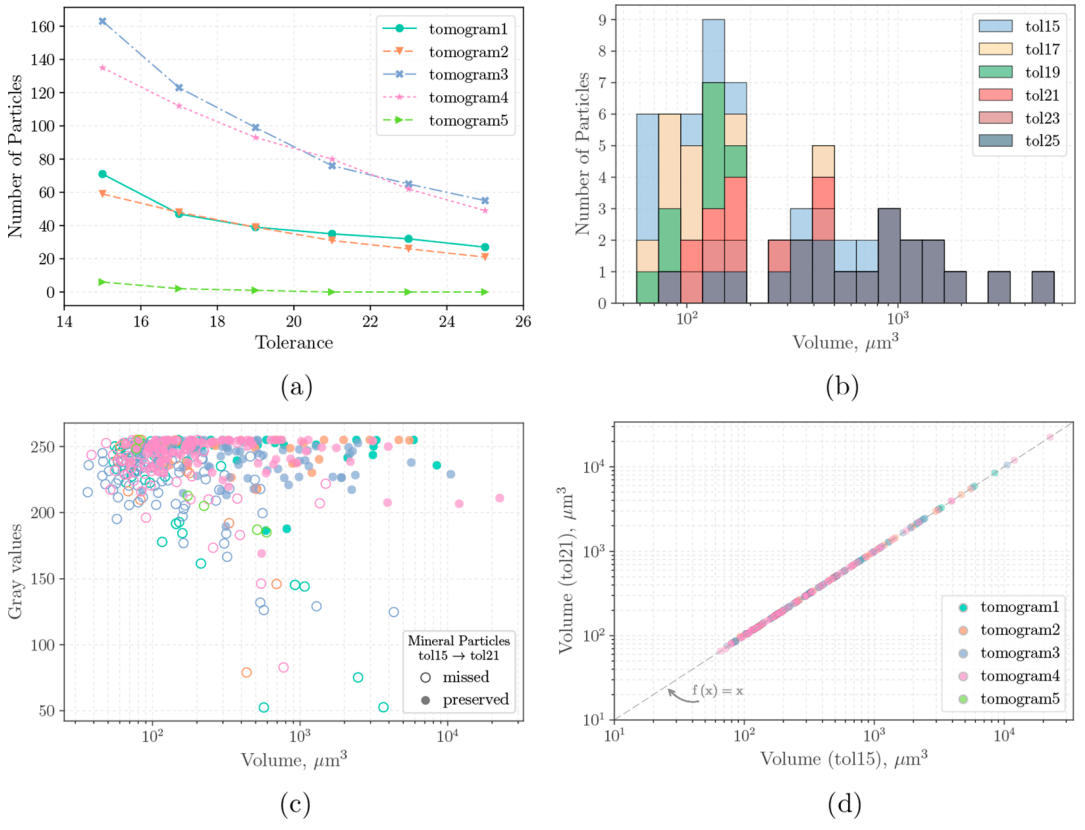

Figure 4. Segmentation of mineral particles with variable tolerance parameter. (a) Number of segmented particles as a function of tolerance in five different tomograms. (b) Distribution of segmented particle volumes for various tolerances in a selected tomogram. (c) Missed and preserved particles from five selected tomograms as the tolerance is changed from 15 to 21. The diagram shows that particles of lower volume and lower contrast (gray intensity) are excluded in the segmentation with tolerance 21. (d) Graph showing that the volume of the segmented particles is independent of the tolerance parameter.

DOI: 10.1021/acs.energyfuels.7b02247
Energy Fuels 2017, 31, 12288−12296

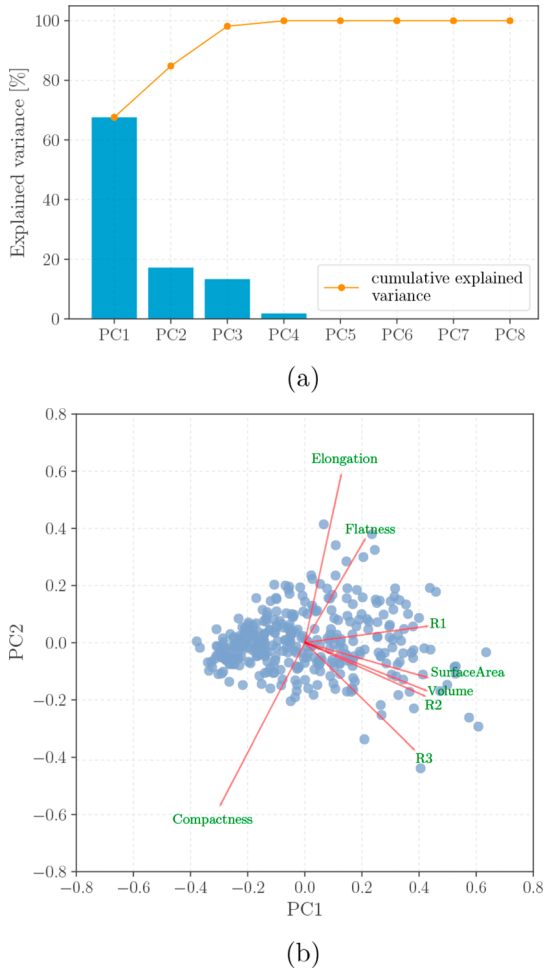

Figure 5. PCA of the mineral particle size and shape attributes: (a) PCA-explained variance and (b) loadings (lines) and scores (dots) in the PC1PC2 plot.

with X-ray fluorescence microscopy,[29] P, S, K, Ca, Si, Cu, and Zn were chemical elements observed to be distributed in the cell walls, while hotspots of elevated concentrations of Si and Ca were also observed and attributed to mineral particles. Microtomography can detect the mineral particles, but it is blind to the distributed minerals. Furthermore, minerals in biomass can be constitutive of the plants as well as extraneous impurities. In sugar cane bagasse, soil contamination is known to be very common. Sugar cane harvest brings some dirt with the sugar cane stalks, and part of the dirt ends up impregnated into the bagasse. The mineral content is usually measured as a percentage of ash, following standard methods based on biomass high-temperature dry oxidation.[30] A survey with 60 bagasse samples from Brazilian mills showed ash contents (dry basis) varying from 1.14 to 5.96%, with an average of 2.84%.[31] The bagasse of this study has 2.8% ash, which is therefore representative of sugar cane bagasse in the relevant industrial conditions.

Mineral particles are readily observed in the native grayscale images because the mineral particles present a higher contrast compared to the air and cell walls (Figure 3). This characteristic leads to relatively easy image segmentation of the mineral particles. Our segmentation procedure has an adjustable parameter, the dynamic value (tolerance), which must be adjusted for optimal mineral particle segmentation.

Five selected tomograms were analyzed with the tolerance parameter varying from 15 to 25. The number of mineral particles found by the algorithm significantly decreases as the tolerance increases (Figure 4a). Analysis of the distribution of mineral particle sizes reveals that increasing the tolerance parameter results in preferential loss of the smaller mineral particles (Figure 4b). By considering both particle size and gray value, we observe that increasing tolerance (15 → 21) preferentially excludes particles of lower volume and lower contrast (Figure 4c). However, when one looks at segmented particle parameters, such as volume (Figure 4d), one observes that they remain unaltered by the choice of tolerance. Therefore, the optimal choice of tolerance is a compromise. Too high tolerance excludes real mineral particles, while too low tolerance includes false particles that are segmentation artifacts. Weighting this compromise, we chose tolerance 21 as optimal. With this tolerance, the segmented particles have high contrast (gray level greater than ≈170) and size (volume) cutoff of about $\sim 10^2$ μm^3 (Figure 4c). Within these limits, the number of false particles is expected to be negligible, although some small but real particles will be excluded from the analysis. With this tolerance, a total of 353 mineral particles were segmented in the 20 bagasse particles. These 353 mineral particles are analyzed henceforth. Computation details can be found in the Supporting Information.

3.3. Mineral Particle Size and Shape. Several attributes of mineral particle size (volume, surface area, R_1, R_2, and R_3) and shape (compactness, elongation, and flatness) were

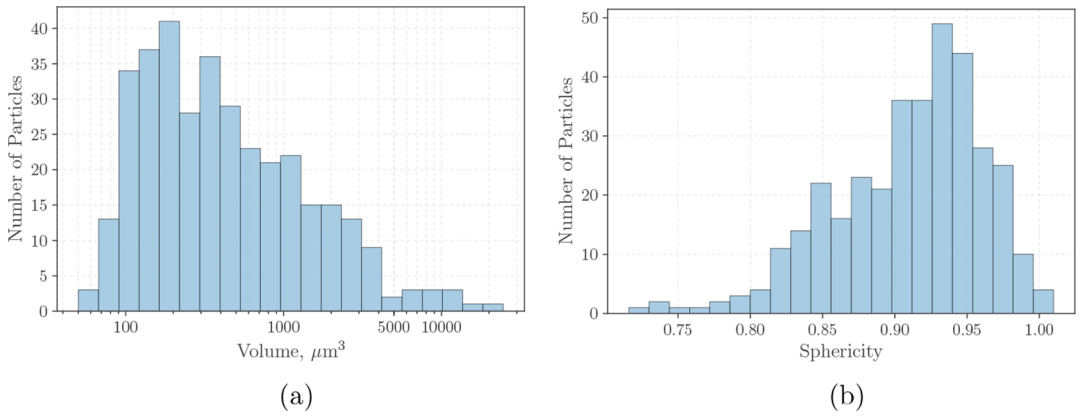

Figure 6. Distributions of (a) volume and (b) sphericity for the segmented mineral particles.

DOI: 10.1021/acs.energyfuels.7b02247
Energy Fuels 2017, 31, 12288−12296

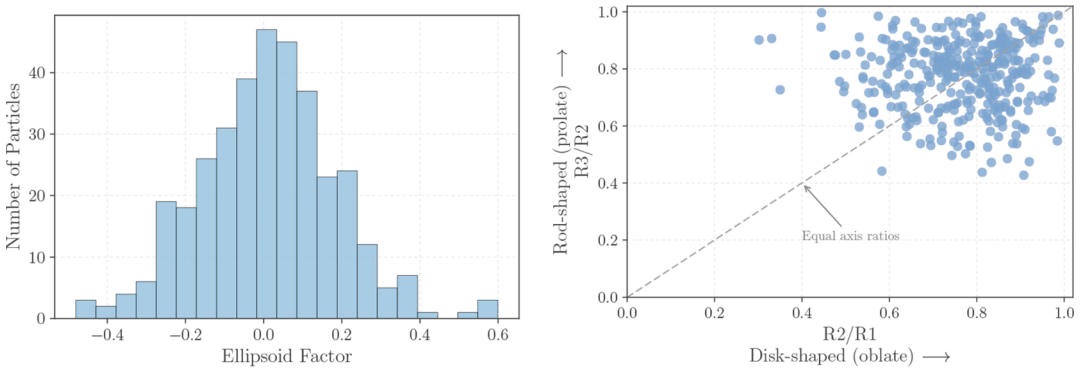

Figure 7. (a) Distribution of EF and (b) Flinn diagram.

Table 2. Matrix of Mineral Particle Localization[a]

	macro location			
cell type	external surface	crack surface	tissue interior	total (all macro locations)
parenchyma (round)	4	14	33	51
parenchyma (smashed)	8	26	37	71
VB fibers	0	0	8	8
xylem vessel	0	2	2	4
epidermis region	5	0	2	7
undetermined	117	90	5	212
total (all cell types)	134	132	87	353

[a]Each one of the 353 mineral particles was classified in terms of the cell type and macro location.

calculated with the MorphoLibJ library. To have a multivariate glance on these attributes, principal component analysis (PCA)[32,33] was performed. Logarithm of the size attributes and standardization (mean = 0 and variance = 1) of all of the attributes were used as data preparation for PCA. Combined PC1 and PC2 explains 86% of the variance (Figure 5a), and hence, our analysis focuses on the PC1PC2 plot (Figure 5b). Clearly, PC1 explains mainly the size attributes (volume, surface area, R_1, R_2, and R_3), while PC2 has a strong influence of shape attributes (compactness, elongation, and flatness). Scores of the PC1PC2 plot show no evidence of clustering. In summary, PCA reveals a single class of particles, with quite independent variations in size and shape.

Distributions of mineral particle volume and sphericity are shown in Figure 6, representing distributions of size and shape, respectively. Volumes range from 50 to 20 000 μm^3. It is worth recalling that the lower size limit is highly influenced by the image acquisition and processing; it is the minimum size reliably detected and segmented by the employed procedures. Most likely, there are more particles close to and below the lower size limit. On the other hand, the upper size limit likely depends upon the source of the mineral particles. In principle, spurious particles could be larger than the observed limit. When the cubic root of those limits $[(50\ \mu m^3)^{1/3}$ and $(20\,000\ \mu m^3)^{1/3}]$ is taken, linear dimensions of 4−27 μm are obtained. This size range serves for comparison, for example, with the internal diameter of the bagasse cells, which are in a similar size range. As for the sphericity index, it must be between 0 and 1, being exactly 1 for spherical objects. The sphericity index calculated with MorphoLibJ is distributed from 0.7 to 1.0, indicating mineral particles of high sphericity. Noteworthy, the range of sphericity is shifted to 0.55−0.7 when calculation is performed with a different method (see the Supporting Information).

Another interesting parameter to analyze particle shape is the EF, introduced by Doube[27] for measuring the rod- or disk-like nature of porous and solid objects. An extremely oblate (disk-shaped) ellipsoid has an EF of −1, with one short axis and two long axes. An extremely prolate (rod-shaped) ellipsoid has an EF of +1, with one long axis and two short axes. EF of 0 indicates some intermediate ellipsoids with both axes ratios being equal. A sphere is a special case with EF = 0, where the three axis lengths are equal. The distribution of EF (Figure 7a) is shown alongside a Flinn diagram (Figure 7b), which displays how much particles are described by ellipsoids of particular axis ratios. The Flinn diagram is widely used in structural geology, and it is a useful method for displaying finite strain ellipsoid geometries.[34] It can be observed that the EF histogram approaches a normal distribution with zero mean, which indicates that most of the analyzed particles have intermediate shapes between "disk" and "rod", with preference for more spherical shapes. This is better appreciated in Figure 7b. Perfect spheres would populate the top right corner of the graph. One observes the cloud of data points with some preference for the top right corner of the plot, but this preference comes alongside significant data dispersion. It can be concluded that the particles have a distribution of shapes with preference to some limited degree of sphericity but no preference for disk- or rod-shaped particles.

3.4. Mineral Particle Localization. The macro location of each mineral particle was classified as follows: external surface, crack surface, or tissue interior. These three categories contained similar percentages of the total number of mineral particles: 38, 37, and 25%, respectively (135, 133, and 88 particles; see Table 2). For mineral particles at external and crack surfaces, most of the cell types remained undetermined because cell identification is often ambiguous. On the other hand, most of the 88 particles inside tissues were unambiguously assigned to parenchyma cells, in either cells preserving their round shape (33 mineral particles) or smashed cells (38 mineral particles). These results suggest that accessibility is a critical determinant of the mineral particle location. More concretely, external surfaces are directly accessible from the outside environment, while crack surfaces are also accessible if mineral particles are smaller than the crack

DOI: 10.1021/acs.energyfuels.7b02247
Energy Fuels 2017, 31, 12288−12296

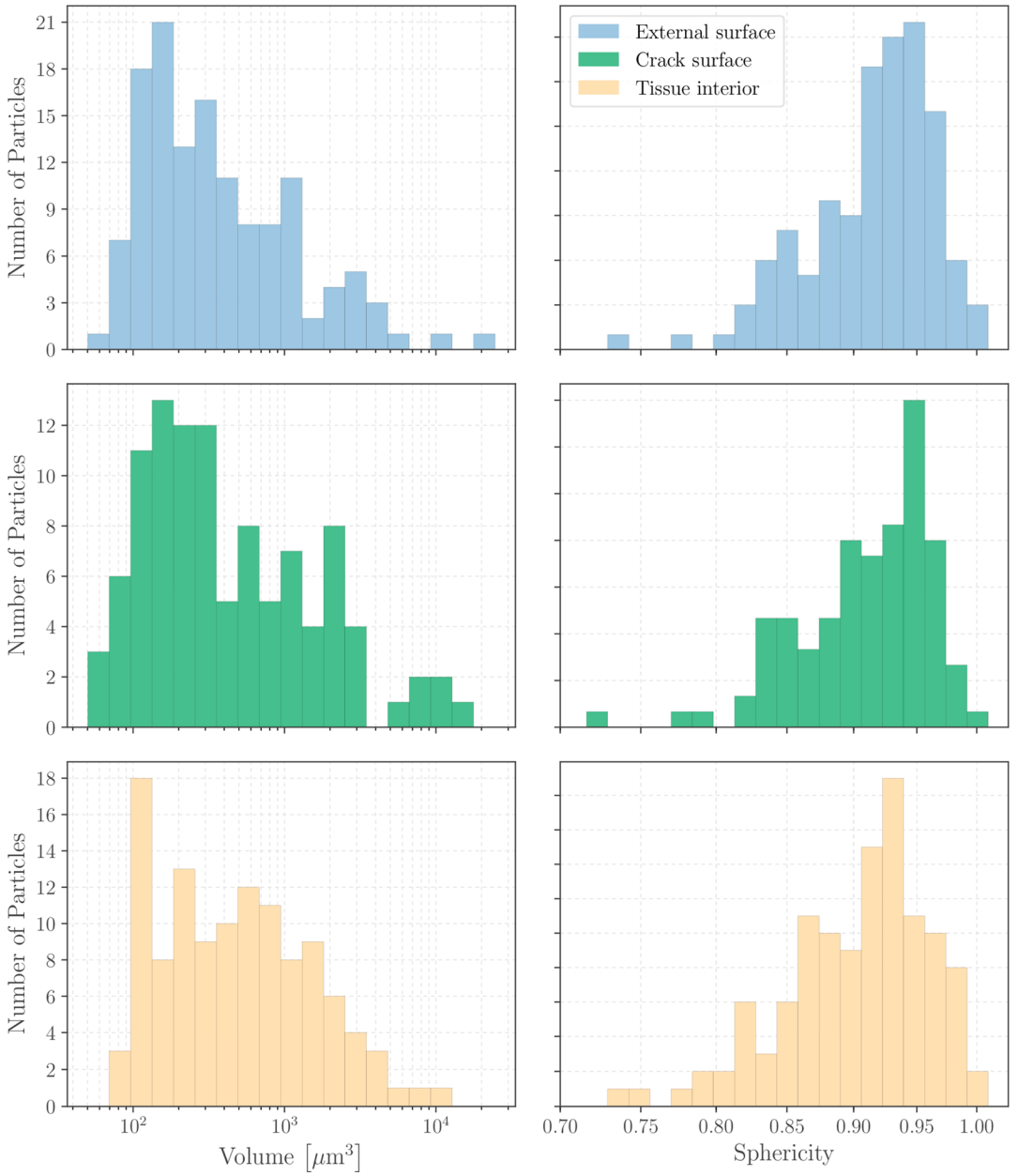

Figure 8. Volume and sphericity distributions of mineral particles in the three different macro locations.

gap. As for the accessibility of parenchyma, most of the cells are presumably ruptured because this is the objective of shredding and crushing the sugar cane stalks at the mill, to extract the cane juice. Hence, the interior of most parenchyma cells is presumably accessible. On the other hand, regions of constrained accessibility, such as fibers of VBs, show a relatively small number of mineral particles (Table 2).

Because mineral particles are distributed in three different macro locations, one may ask whether sizes and shapes vary among the locations. The volume and sphericity distributions for each macro location are remarkably similar (Figure 8). This is additional evidence that mineral particles can be thought as a single class of particles without any remarkable correlation between the size, shape, and location. As a speculation, we attribute this randomized character to the liquid reabsorption taking place in sugar cane crushing.[1] As the roller mills press the shredded stalks, liquid is expelled from the biomass particles, to be partly reabsorbed (bringing mineral particles) as the roller pressure is released. The environment of squeezed liquid is one where mineral particles could mix, which we speculate to be the source of the randomization. If this speculation is correct, the preferential locations are those sites capable of trapping mineral particles coming from external environments.

It is important to make some considerations about the possible origins of the mineral particles. Microtomography alone cannot demonstrate if they are biogenic or impurities coming from soil. Nevertheless, industrial experience has indicated soil as the primary source, and the problem of minerals is often (and imprecisely) referred to as the "sand" problem. Noteworthy, soil texture is classified on the basis of particle sizes. For instance, the NBR 6502/95 classification discriminates clay (<2 μm), silt (2−60 μm), and sand (from 60 μm to 2 mm). The range of mineral particles observed in bagasse (Figures 1c, 3, 6a, and 8) is consistent with silt but not with sand, and clay particles would be too small to be detected.

DOI: 10.1021/acs.energyfuels.7b02247
Energy Fuels 2017, 31, 12288−12296

Furthermore, many sand particles would be too big to penetrate the structure of biomass particles. Hence, in the discussion of mineral particles trapped in biomass, one should always compare the size of the minerals to the sizes of the biomass features (e.g., cells, tissue cracks, and wall fragments). Such size comparisons can provide key insights about the origin, mineralogy, and possible strategies for cleaning the mineral particles from the biomass.

4. CONCLUSION

In this work, we employed synchrotron X-ray microtomography to analyze mineral particles in sugar cane bagasse. Size, shape, and location of mineral particles were determined. Results were consistent with a single class of mineral particles without any remarkable correlation between their size, shape, and location. Particle volumes were observed in the range from $\sim 10^2$ to 10^4 μm^3. Shapes showed some limited tendency for spherical particles, without tendency for rod- or disk-shaped particles. The location was consistent with mineral particle spatial distribution limited by accessibility, because most of the mineral particles were found at sites accessible from the outside environment, namely, at external biomass surfaces, at internal surfaces of tissue cracks, and inside ruptured parenchyma cells. These results demonstrate that microtomography can provide valuable insights for the design of novel biomass cleaning strategies aiming at improving feedstock quality for combustion and biorefining.

■ ASSOCIATED CONTENT

Supporting Information

The Supporting Information is available free of charge on the ACS Publications website at DOI: 10.1021/acs.energyfuels.7b02247.

Implementation of morphological segmentation in Python, comparison of sphericity calculation with the MorphoLibJ and 3D ImageJ Suite libraries, and image processing time (PDF)

Video of the rind particle (MPG)

Video of the segmented mineral particles in the rind particle (MPG)

■ AUTHOR INFORMATION

Corresponding Author

*Telephone: +55-19-3518-3180. E-mail: carlos.driemeier@ctbe.cnpem.br.

ORCID

Carlos Driemeier: 0000-0002-4794-3714

Notes

The authors declare no competing financial interest.

■ ACKNOWLEDGMENTS

CNPq and FAPESP (Grants 2015/01587-0 and 2017/01330-5) are acknowledged for the financial support. LNLS is acknowledged for the microtomography beamtime (Proposal IMX 20160061). Information Technology Superintendence of the University of São Paulo is acknowledged for the high-performance computing resources. Bruna Goes is acknowledged for her work in preliminary versions of this study.

■ REFERENCES

(1) Hugot, E. *Handbook of Cane Sugar Engineering*; Elsevier; Amsterdam, Netherlands, 1986; Sugar Technology Series, Vol. 7.

(2) Rasul, M. G.; Rudolph, V.; Carsky, M. *Fuel* **1999**, *78* (8), 905–910.

(3) Driemeier, C.; Oliveira, M. M.; Mendes, F. M.; Gómez, E. O. *Powder Technol.* **2011**, *214* (1), 111–116.

(4) Triana, O.; Leonard, M.; Saavedra, F.; Fernández, N.; Gálvez, G.; Peña, E. *Atlas del Bagazo de la Caña de Azúcar (Atlas of Sugarcane Bagasse)*; GEPLACEA/PNUD: Mexico City, Mexico, 1990; Diversificación.

(5) Junqueira, T. L.; Chagas, M. F.; Gouveia, V. L. R.; Rezende, M. C. A. F.; Watanabe, M. D. B.; Jesus, C. D. F.; Cavalett, O.; Milanez, A. Y.; Bonomi, A. *Biotechnol. Biofuels* **2017**, *10* (1), 50.

(6) Ragauskas, A. J.; Beckham, G. T.; Biddy, M. J.; Chandra, R.; Chen, F.; Davis, M. F.; Davison, B. H.; Dixon, R. A.; Gilna, P.; Keller, M.; Langan, P.; Naskar, A. K.; Saddler, J. N.; Tschaplinski, T. J.; Tuskan, G. A.; Wyman, C. E. *Science* **2014**, *344* (6185), 1246843.

(7) Lynd, L. R.; Liang, X.; Biddy, M. J.; Allee, A.; Cai, H.; Foust, T.; Himmel, M. E.; Laser, M. S.; Wang, M.; Wyman, C. E. *Curr. Opin. Biotechnol.* **2017**, *45*, 202–211.

(8) Miles, T. R.; Miles, T. R.; Baxter, L. L.; Bryers, R. W.; Jenkins, B. M.; Oden, L. L. *Biomass Bioenergy* **1996**, *10* (2), 125–138.

(9) Shao, Y.; Wang, J.; Preto, F.; Zhu, J.; Xu, C. *Energies* **2012**, *5* (12), 5171–5189.

(10) Gabra, M.; Pettersson, E.; Backman, R.; Kjellström, B. *Biomass Bioenergy* **2001**, *21* (5), 351–369.

(11) Wu, H.; Glarborg, P.; Frandsen, F. J.; Dam-Johansen, K.; Jensen, P. A. *Energy Fuels* **2011**, *25* (7), 2862–2873.

(12) de Lima, D. R.; Silveira, M. H. L.; Del Rio, L.; Ramos, L. P. In *Green Fuels Technology: Biofuels*; Soccol, C. R., Brar, S. K., Faulds, C., Ramos, L. P., Eds.; Springer International Publishing: Cham, Switzerland, 2016; pp 107–131, DOI: 10.1007/978-3-319-30205-8_5.

(13) Steppe, K.; Cnudde, V.; Girard, C.; Lemeur, R.; Cnudde, J.-P.; Jacobs, P. *J. Struct. Biol.* **2004**, *148* (1), 11–21.

(14) Forsberg, F.; Mooser, R.; Arnold, M.; Hack, E.; Wyss, P. *J. Struct. Biol.* **2008**, *164* (3), 255–262.

(15) Brodersen, C. R.; Lee, E. F.; Choat, B.; Jansen, S.; Phillips, R. J.; Shackel, K. A.; McElrone, A. J.; Matthews, M. A. *New Phytol.* **2011**, *191* (4), 1168–1179.

(16) Isaac, A.; Sket, F.; Driemeier, C.; Rocha, G. J. M. *Ind. Crops Prod.* **2013**, *49*, 790–793.

(17) Schubert, G.; Vasconcelos, G. J. Q.; Dias, C. S.; Archilha, N. L.; Miqueles, E. X.; O'Dowd, F. P. *IMX Beamline: X-ray Imaging, Version 0.1*; Laboratório Nacional de Luz Síncrotron (LNLS), Centro Nacional de Pesquisa em Energia e Materiais (CNPEM): Campinas, Brazil, 2017.

(18) Mirone, A.; Brun, E.; Gouillart, E.; Tafforeau, P.; Kieffer, J. *Nucl. Instrum. Methods Phys. Res., Sect. B* **2014**, *324*, 41–48.

(19) Chilingaryan, S.; Mirone, A.; Hammersley, A.; Ferrero, C.; Helfen, L.; Kopmann, A.; does Santos Rolo, T.; Vagovic, P. *IEEE Trans. Nucl. Sci.* **2011**, *58* (4), 1447–1455.

(20) Maire, E.; Withers, P. J. *Int. Mater. Rev.* **2014**, *59* (1), 1–43.

(21) Landis, E. N.; Keane, D. T. *Mater. Charact.* **2010**, *61* (12), 1305–1316.

(22) Schindelin, J.; Arganda-Carreras, I.; Frise, E.; Kaynig, V.; Longair, M.; Pietzsch, T.; Preibisch, S.; Rueden, C.; Saalfeld, S.; Schmid, B.; Tinevez, J.-Y.; White, D. J.; Hartenstein, V.; Eliceiri, K.; Tomancak, P.; Cardona, A. *Nat. Methods* **2012**, *9* (7), 676.

(23) Abràmoff, M. D.; Magalhães, S. J. R. P. J. *Biophotonics Int.* **2004**, *11* (7), 36–42.

(24) Legland, D.; Arganda-Carreras, I.; Andrey, P. *Bioinformatics* **2016**, *32* (22), 3532.

(25) Ollion, J.; Cochennec, J.; Loll, F.; Escudé, C.; Boudier, T. *Bioinformatics* **2013**, *29* (14), 1840.

(26) Andrey, P.; Kiêu, K.; Kress, C.; Lehmann, G.; Tirichine, L.; Liu, Z.; Biot, E.; Adenot, P.-G.; Hue-Beauvais, C.; Houba-Hérin, N.; Duranthon, V.; Devinoy, E.; Beaujean, N.; Gaudin, V.; Maurin, Y.; Debey, P. *PLoS Comput. Biol.* **2010**, *6* (7), e1000853.

DOI: 10.1021/acs.energyfuels.7b02247
Energy Fuels 2017, 31, 12288–12296

(27) Doube, M. *Front. Endocrinol.* **2015**, *6*, 15.
(28) Salmon, P. L.; Ohlsson, C.; Shefelbine, S. J.; Doube, M. *Front. Endocrinol.* **2015**, *6*, 162.
(29) Badger, J.; Lal, J.; Harder, R.; Inouye, H.; Gleber, S. C.; Vogt, S.; Robinson, I.; Makowski, L. *Sci. Rep.* **2013**, *3*, 2843.
(30) Sluiter, A.; Hames, B.; Ruiz, R.; Scarlata, C.; Sluiter, J.; Templeton, D. *Determination of Ash in Biomass*; National Renewable Energy Laboratory (NREL): Golden, CO, 2008; Laboratory Analytical Procedure (LAP), Technical Report NREL/TP-510-42622, pp 5.
(31) de Moraes Rocha, G. J.; Nascimento, V. M.; Gonçalves, A. R.; Silva, V. F. N.; Martín, C. *Ind. Crops Prod.* **2015**, *64*, 52−58.
(32) Varmuza, K.; Filzmoser, P. *Introduction to Multivariate Statistical Analysis in Chemometrics*; CRC Press: Boca Raton, FL, 2016.
(33) Anderson, T. W. *An Introduction to Multivariate Statistical Analysis*; Wiley: Hoboken, NJ, 2003; Wiley Series in Probability and Statistics.
(34) Flinn, D. *Q. J. Geol. Soc. London* **1962**, *118* (1−4), 385−428.

DOI: 10.1021/acs.energyfuels.7b02247
Energy Fuels 2017, 31, 12288−12296